nature nanotechnology

Article

https://doi.org/10.1038/s41565-025-01984-3

# High-order dynamics in an ultra-adaptive neuromorphic vision device

Received: 2 January 2025

Accepted: 26 June 2025

Published online: 15 August 2025

Check for updates

Jiayi Xu[1,5], Biyi Jiang[1,2,5], Weizhen Wang[2,5], Zhifeng Guo[1], Junsen Gao[1], Xinyan Hu[1], Jingkai Qin[3], Liang Ran[4], Longyang Lin[1], Songhua Cai[2] ✉, Yida Li[1] ✉ & Feichi Zhou[1] ✉

Neuromorphic hardware for artificial general vision intelligence holds the potential to match and surpass biological visual systems by processing complex visual dynamics with high adaptability and efficiency. However, current implementations rely on multiple complementary metal–oxide–semiconductor or neuromorphic elements, leading to significant area and power inefficiencies and system complexity. This is owing to a key challenge that no single electronic device, to our knowledge, has yet been demonstrated that can integrate retina-like and cortex-like spiking and graded neuronal dynamics operable across both optical and electrical domains. Here we report a single ultra-adaptive neuromorphic vision device ($I_xT_yO_{1-x-y}$/$CuO_x$/Pd) by ingeniously tailoring its electronic properties, enabling uniquely controlled interface and bulk dynamics by charged particles, including electrons, oxygen ions and vacancies. The device highly amalgamates broadband retinal spiking neuron and non-spiking graded neuron, and cortical synapse and neuron dynamics, with ultralow power consumption. Real-time optoelectronic dynamics is elucidated through in situ scanning transmission electron microscopy and validated by technology computer-aided design simulations. An artificial general vision intelligence system based on homogeneous ultra-adaptive neuromorphic vision device arrays is constructed, adaptively supporting both asynchronous event-driven and synchronous frame-driven paradigms for versatile cognitive imaging demands, with superior power efficiency of up to 67.89 trillion operations per second per watt and area efficiency of up to 3.96 mega operations per second per feature size (MOPS/$F^2$).

Nature presents multidynamics and unpredictability of visual events, posing immense challenges for conventional machine vision systems. Artificial general vision intelligence (AGVI) has emerged as a promising paradigm that seeks to replicate the full-spectrum dynamics in biological visual systems within a unified hardware system. Such vision systems achieve remarkable efficiency and adaptability by mimicking the diverse signal modalities in retinal and cortical neurons, including action potentials (all or nothing) and graded potentials (proportional to stimulus)[1–4], which are operable in both optical and electrical dimensions.

State-of-the-art approaches to AGVI rely on the heterogeneous integration of complementary metal–oxide–semiconductor circuits[5] or emerging neuromorphic circuit elements[6–8]. However, this leads to a bulky system with limited adaptability and power efficiency. Although multimodal neuromorphic vision devices hold the potential for a closer emulation of biological visual systems, current state-of-the-art

A full list of affiliations appears at the end of the paper. ✉e-mail: songhua.cai@polyu.edu.hk; liyd3@sustech.edu.cn; zhoufc@sustech.edu.cn

devices can only emulate the dynamics in partial visual-based neurons; more critically, high-order and multi-dimensional dynamics cannot be realized within the same single device and require the integration of multiple devices[6–8]. The question now lies in how we can, hardware wise, integrate all these sophisticated dynamics of the retina and cortex into a single electronic element, thereby elegantly transforming multiple elements in the AGVI system into a highly homogeneous one, for unprecedented efficiencies and functionalities.

Here we report an ultra-adaptive neuromorphic vision (UANV) device that integrates retina-like and cortex-like spiking and graded neuronal dynamics operable across both optical and electrical domains. Leveraging the advanced in situ scanning transmission electron microscopy (STEM) characterization and technology computer-aided design simulation approaches, physical elucidation of high-order dynamics and working principles of the UANV device have been achieved as guidance for future implementation. Integrating such multi- and high-order dynamics devices into a highly compact and efficient AGVI system unlocks numerous possibilities for machine vision paralleled to biological vision.

## UANV device with four modes

The UANV device is designed for integrating the core dynamics of retinal and cortical neurons with a single two-terminal stack of $I_xT_yO_{1-x-y}/CuO_x$/Pd, enabling multicross-paradigm processing (spiking/non-spiking/in-sensor/in-memory; Fig. 1a). The optical microscopy image of the device is shown in Supplementary Fig. 1. The $CuO_x$ layer is designed with oxygen-deficient characteristics, whereas the $I_xT_yO_{1-x-y}$ layer is engineered to be In rich, which are confirmed by the X-ray photoelectron spectroscopy spectra (Supplementary Fig. 2). Four visual neuronal dynamics are realized in the UANV device, including broadband retinal spiking neuron (RSN) at 0 V, broadband retinal graded neuron (RGN) dynamics from −0.04 V to −0.1 V, cortical synapse at 0.1 to 0.5 V and cortical neuron dynamics at 1.3 to 2 V (Fig. 1b,c). The rich and tuneable high-order dynamics originate from the unique energy band diagram, characterized by ultraviolet photoelectron spectroscopy, ultraviolet–visible spectroscopy, absorbance and transmission spectra (Supplementary Figs. 3–7 and Supplementary Note 1), as well as charge particle (electrons, oxygen ions and vacancies) modulation in the bulk or at the interface under light and electrical stimulations. The UANV device single-handedly melds the same functionalities achievable only with more than 60 devices when implemented by a complementary metal–oxide–semiconductor approach[9–13], dramatically reducing the devices required when the image size increases and transforming the conventional heterogeneous system into a fully homogeneous and compact one (Extended Data Fig. 1). Leveraging the highly integrated dynamics and ultralow power consumption in each mode[6,14–20] (Supplementary Table 1), a highly efficient vision hardware system is then constructed with the all-homogeneous UANV device array, with capability in dynamically allocating different device dynamic proportions to enable different scenario processing on a unified platform (Fig. 1d).

## RSN dynamics

The RSN dynamics is accessed at zero bias, featuring bias-free, capacitor-free and broadband photoresponsive leaky integrate-and-fire (LIF) neuron spiking, in contrast to a conventional approach in which complex circuitry is required[14–16,21,22] (Extended Data Table 1). The device in RSN dynamics can directly convert and encode continuous light illumination into current spikes, showing light intensity-based and illumination time-based threshold spiking features (Fig. 2a); the baseline photocurrent is due to the photovoltaic effect (Supplementary Fig. 8 and Supplementary Note 2). When the light illumination duration reaches a threshold, a current spike is generated, which is termed as the firing process. The LIF spiking behaviours can be flexibly tuned with different illumination wavelengths and intensities (Fig. 2b–d), where light wavelengths of 375/520/1,064 nm are used, respectively. The intensity threshold firing is clearly seen with no spiking when light intensity is below 0.05 μW μm$^{-2}$. Figure 2e shows the spiking amplitudes as a function of light intensity for wavelengths of 375/450/520/638/1,064 nm. The spiking current first increases from a wavelength of 300 nm, reaching a peak value at around 540 nm, and then decreases gradually with increasing wavelengths, correlating with the absorption and transmission behaviours of the $I_xT_yO_{1-x-y}$ and $CuO_x$ layers (Supplementary Fig. 5). The firing process occurs within a range of −0.01 V to 0.02 V and is inhibited otherwise, owing to the inability to accumulate trap electrons outside this operating range (Fig. 2f). Further characterization of the stability of the RSN dynamics can be found in Supplementary Figs. 9–12 and Supplementary Note 3.

The photo-spiking mechanism of the device is due to the charging/discharging of electrons at the $I_xT_yO_{1-x-y}/CuO_x$ interfacial trap states, assisted by Fowler–Nordheim tunnelling of the electrons from the inverted triangular well trap formed at the $CuO_x$ side (Fig. 2g–i). When the incident light interacts with the $CuO_x$ layer, part of the generated electrons gets swept across to the $I_xT_yO_{1-x-y}$ electrodes, forming the baseline current. The rest of the generated electrons funnel down to the interface trap states from the triangular well, reducing the effective barrier height and width. When the effective barrier height and width become low enough, the large tunnelling probability of the photoexcited electrons from the trap states causes a sudden rush of current, enabling the firing process. This effect can be analytically calculated by the Fowler–Nordheim tunnelling probability as a function of the barrier width (Fig. 2j), where a threshold barrier width of ~20 Å and a tunnelling probability of 0.1 are defined at the onset of firing. Subsequently, the net-doping effect and band bending are reversed, recovering the device for the next firing process. Further explanations of the photo-spiking mechanism are provided in Supplementary Note 4.

Systematic studies of the spiking behaviours under different voltage biases with the corresponding energy band diagrams are provided to further prove the photo-spiking mechanism (Supplementary Figs. 13 and 14 and Supplementary Note 5). The device area-dependent and temperature-dependent RSN dynamics are also investigated (Supplementary Figs. 15 and 16 and Supplementary Note 6), agreeing with the proposed mechanism. A technology computer-aided design simulation using Sentaurus was used to model the firing process, complete with the characterized material property parameters and complex refractive indexes (Supplementary Fig. 17). The results including the energy band diagrams of the device stack at thermal equilibrium and after electron accumulation at the trap states under light illumination are in excellent agreement with our proposed mechanism (Fig. 2k). Details of the simulation are provided in the Methods section.

## RGN dynamics

The RGN dynamics is accessed within a bias from −0.04 V to −0.1 V. In this dynamics, the device demonstrates retinal non-spiking graded neuron behaviours, including nonlinear, light-dosage dependent and wavelength-tuneable short-term temporal dynamics. First, the device in RGN dynamics exhibits a typical paired-pulse facilitation effect (Supplementary Fig. 18). When the pulse number is further increased, the current rises continuously under illumination and then exhibits nonlinear relaxation over time after the light is removed (Fig. 3a). Both current amplitude and relaxation time increase with more pulses. A similar behaviour can be seen when varying light intensities are used, with a more pronounced effect observed under a higher light intensity (Fig. 3b). The device in RGN dynamics also demonstrates a broadband response (Fig. 3c), with behaviour dictated by the absorption and transmission characteristics (Supplementary Fig. 5). Further broadband and pulse number- and intensity-dependent RGN characterizations are shown in Supplementary Figs. 19–22. In addition, the device in this dynamics also displays good stability and repeatability (Supplementary Figs. 9 and 10).

https://doi.org/10.1038/s41565-025-01984-3

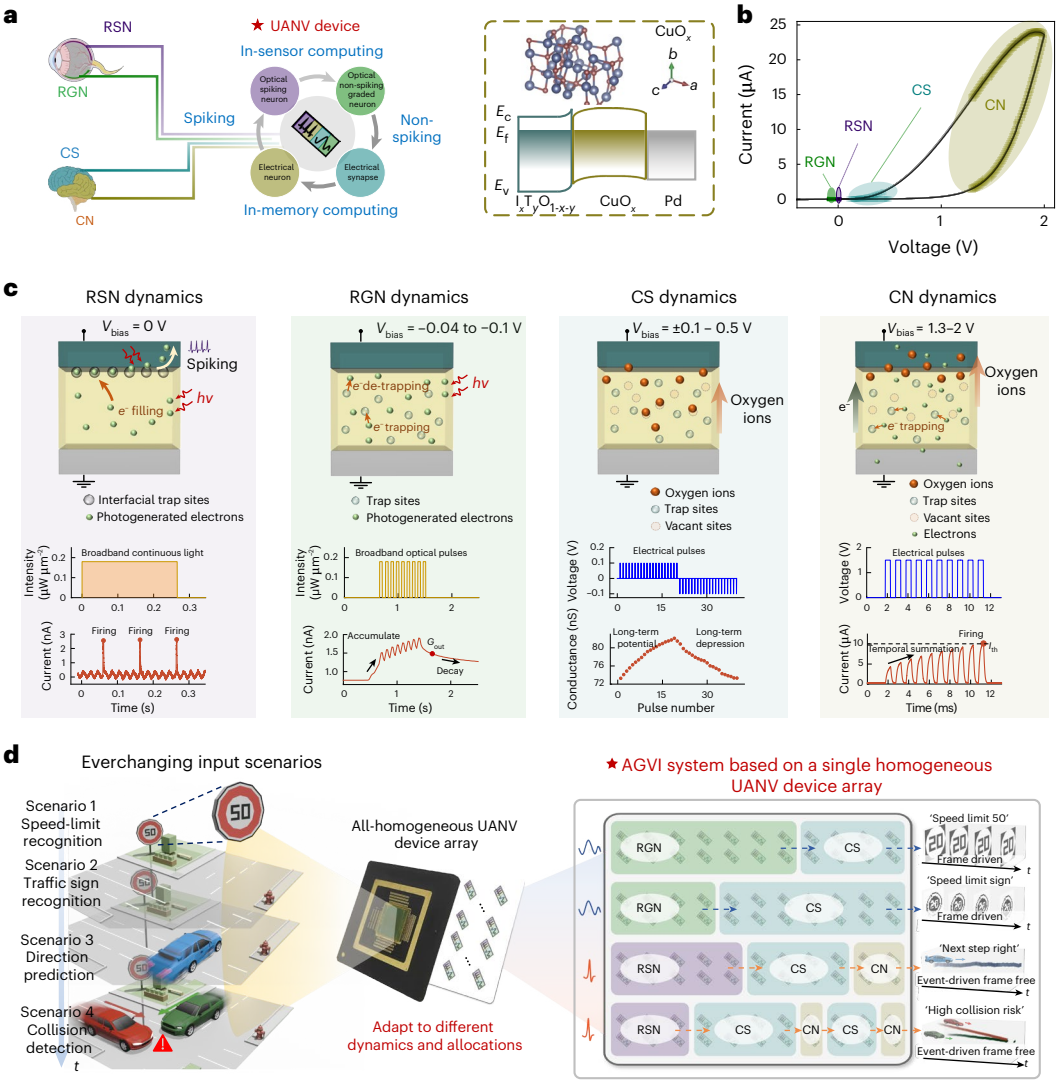


**Fig. 1 | All-homogeneous UANV device-based AGVI. a**, Illustration of UANV device in a structure of $I_xT_yO_{1-x-y}/CuO_x$/Pd, embodying four visual neuronal dynamics and homogenizes the key elements in the retina and cortex, including RSN, RGN, cortical synapse (CS) and cortical neuron (CN). A single UANV device can adaptably perform spiking and non-spiking in-sensor processing (neuromorphic sensing with low- and mid-level processing) and in-memory processing (cognitive high-level processing). **b**, Four visual neuronal dynamics realized in the UANV device, including RSN dynamics at 0 V, RGN dynamics from −0.04 V to −0.1 V, CS dynamics at 0.1 to 0.5 V and CN dynamics at 1.3 to 2 V. **c**, Schematics of the mechanisms for the four dynamics, achieved by controlled oxygen ion migration and electron trapping/de-trapping dynamics in the bulk or at the interface states under light or electrical stimulation, modulating the energy band transition over a range of voltage regimes. **d**, A highly efficient and compact AGVI system implemented with the homogeneous UANV device array. The system can support ever-changing event-driven and frame-driven scenarios with the highly adaptable, efficient architectures (for example, vehicle attribute-aware collision detection, motion prediction, traffic sign and speed-limit digit recognition). The hardware can intelligently switch between spiking and non-spiking in-sensor computing and in-memory computing cognitive vision architectures by dynamically adapting device dynamics and resource allocations, which enables efficient and accurate processing of diverse scenarios on a unified platform.

The photo-induced dynamics is mainly attributed to the trapping/de-trapping dynamics of electrons in the $CuO_x$ layer (Fig. 3d–f). Under light illumination, electron–hole pairs, as well as de-trapped electrons, are generated within the $CuO_x$ layer. The excess electrons are then directed towards the Pd electrodes under an electric field. When consecutive light pulses are applied, the photocurrent first increases dramatically owing to the large number of photogenerated carriers; the rate of increase gradually slows down because the photogeneration process reaches a steady state and the electron de-trapping from the trap sites becomes saturated[23–26]. On the removal of light illumination, nonlinear current relaxation occurs, where the excess electrons present in the $CuO_x$ layer are re-trapped or recombine with the excess holes. Area-dependent and humidity-dependent measurements are further performed to reinforce the mechanism[27–30] (Supplementary Figs. 12 and 15 and Supplementary Note 3).

The photoresponsive behaviour of the device operating in the RGN dynamics was observed via our light-incorporated in situ STEM approach[31,32] (Fig. 3g). The carrier charge transport processes in the device can be elucidated with time-series electron energy loss spectroscopy (EELS)–STEM, with the acquisition area shown in Fig. 3h. The EELS–STEM datasets for Cu and O were recorded during both photoactivation (light on) and recovery states (light off). From the EELS elemental mapping and the corresponding intensity line profiles of Cu and O (Fig. 3i), there is a negligible change in the distribution of O and Cu throughout the device after light illumination, consistent with the subtle variation in the energy-loss near-edge structure of O K-edges during illumination and recovery cycles (Fig. 3j), indicating

https://doi.org/10.1038/s41565-025-01984-3

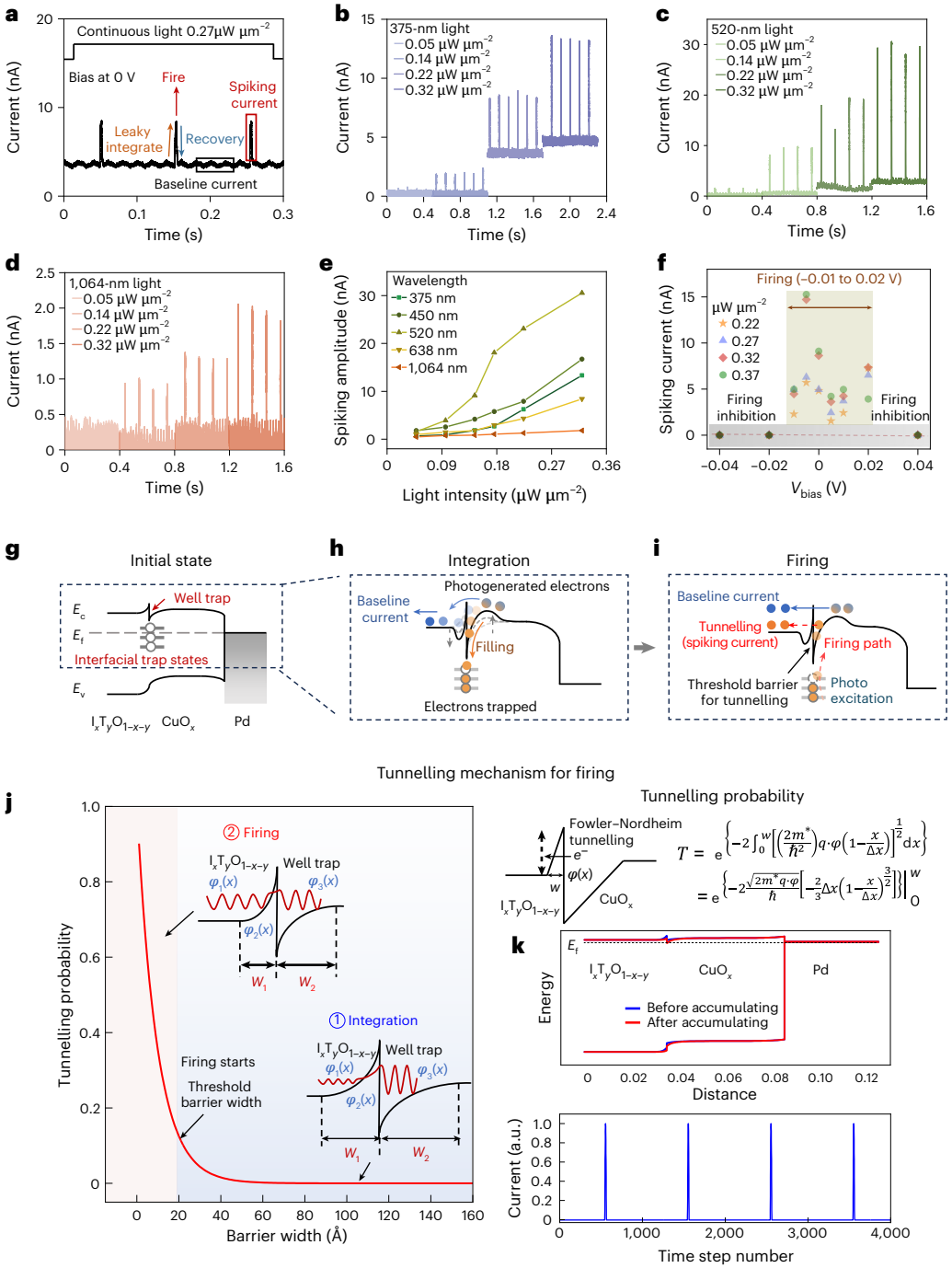


**Fig. 2 | UANV device operating in the RSN dynamics. a**, Photoresponsive LIF spiking characteristics of the device ($V_{bias}$ = 0 V, $V_{read}$ = 0 V) under 375 nm light illumination with an intensity of 0.27 μW μm$^{-2}$. **b**–**d**, LIF spiking behaviours of the device at 375 nm (**b**), 520 nm (**c**) and 1,064 nm (**d**) light illumination. **e**, Spiking amplitude as a function of light intensity at different wavelengths. **f**, Spiking amplitude as a function of applied bias at different light intensities. **g**, Schematic illustrating the initial stage. The energy band diagram at the $I_xT_yO_{1-x-y}/CuO_x$ interface with a triangular barrier at the $I_xT_yO_{1-x-y}$ side and inverted triangular-like well trap at the $CuO_x$ side. **h**, Schematic illustrating the integration stage. During light illumination, photogenerated electrons are guided by the well trap into the interfacial trap states. The accumulation of electrons at the interface trap states causes the energy band of $CuO_x$ to start bending in response to a net doping effect of the filled traps and aids to reduce the effective Schottky barrier height for easier electron tunnelling. **i**, Firing process when the number of trapped electrons reaches a threshold, the $E_f$ value of $I_xT_yO_{1-x-y}$ layer gets pulled down far enough below the $E_f$ value of $CuO_x$, and the effective Schottky barrier height at the $I_xT_yO_{1-x-y}$ side becomes small enough. Meanwhile, the probability of electron tunnelling becomes large enough that a rush of electron starts to get injected from the $CuO_x$ layer into the $I_xT_yO_{1-x-y}$ layer, forming the current spike. **j**, Electron-tunnelling probability as a function of the inverted triangular barrier width at the $I_xT_yO_{1-x-y}$ side, with the tunnelling probability analysed using the Fowler–Nordheim tunnelling model. The start of firing is defined as when the tunnelling probability reaches 0.1. Sentaurus technology computer-aided design simulation results including the energy band diagrams before and after electron accumulation at the interfacial trap states and the simulated electrical behaviours under light illumination are shown, agreeing well with the mechanism.

https://doi.org/10.1038/s41565-025-01984-3

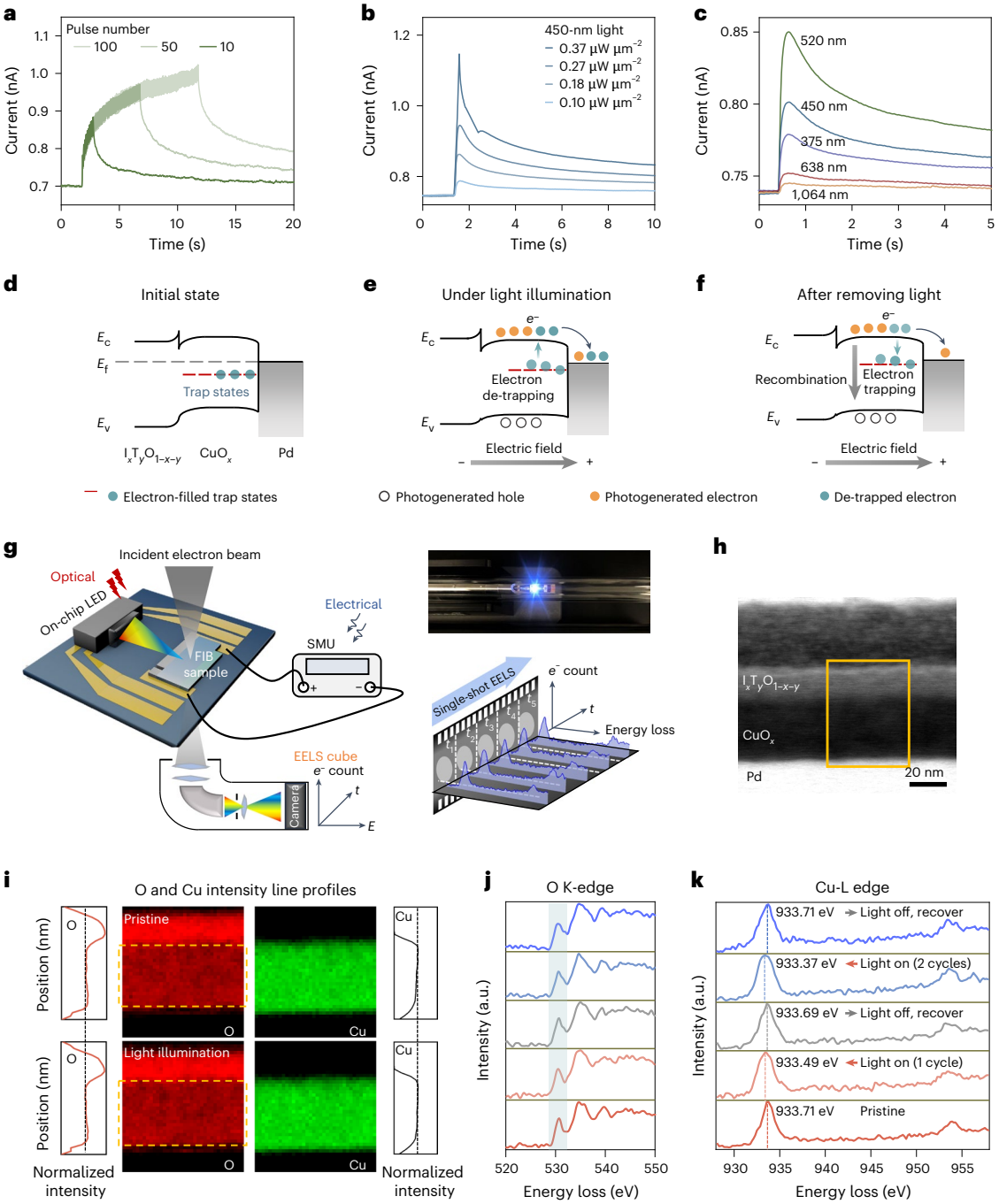


**Fig. 3 | UANV device operating in the RGN dynamics. a**, Current response ($V_{read}$ = 40 mV) under 450 nm light pulse sequence with varying light pulse number (pulse width/interval of 50 ms/50 ms and light intensity of 0.18 μW μm$^{-2}$). **b**, Current response under 450 nm light pulse sequence with a pulse number of 100, pulse width/interval of 0.1 ms/0.1 ms and varying light intensities. **c**, Broadband responses under the light pulse sequence with a pulse number of 100, pulse width/interval of 0.1 ms/0.1 ms and varying wavelengths at a fixed light intensity of 0.18 μW μm$^{-2}$. **d**, Schematic of the RGN dynamics mechanism at the initial stage. The energy band diagram is shown with the presence of trap sites either filled or unfilled with electrons, randomly distributed across the $CuO_x$ layer. **e**, Schematic of the RGN dynamics mechanism under light illumination, where electron–hole pairs, as well as photoexcited de-trapped electrons, are generated within the $CuO_x$ layer. The excess electrons are then directed towards the Pd electrodes with the application of an electric field. **f**, On the removal of light illumination, current relaxation follows, where the excess electrons still present in the $CuO_x$ layer are trapped by the trap sites or recombined with the excess holes. **g**, Schematic showing the in situ STEM setup: the micro-electro-mechanical system chip integrates a micro-LED (470 nm) as the light source and micro-electrodes for electrical measurements. SMU, source measure unit; LED, light-emitting diode. **h**, STEM image of the device with area measured by EELS marked out. **i**, EELS elemental mapping and the corresponding intensity line profiles of O (left) and Cu (right) before and after light illumination, **j**,**k**, O K-edge (**j**) and Cu-L edge (**k**) are plotted at different time steps corresponding to a repeated process of light illumination and when the light illumination is removed for 2 min. The left shift in the Cu-L edge indicates the electrons de-trapping from the trap sites during light illumination, whereas a right shift indicates the re-trapping of electrons after the removal of light illumination.

the negligible oxygen migration. By contrast, a 0.22 eV left shift in the Cu-$L_3$ edge is observed after illumination compared with the pristine state (Fig. 3k), suggesting a lower valence state driven by the accumulation of positive charges[33]. The increase in the positive charges can only come from the de-trapping of electrons due to photo-excitation. After removing the light illumination, the Cu-$L_3$ edge gradually shifts back to a higher energy level, consistent with electrons re-trapping. The entire process is repeated with the same phenomenon observed.

## Cortical synapse dynamics

The cortical synapse dynamics is accessed within a bias of 0.1 V to 0.5 V, displaying analogue and non-volatile electrical resistive switching behaviours. With continuous positive voltage sweeps, the device transits from the high-resistance state (HRS) to the low-resistance state (LRS), and from LRS to HRS under negative voltage sweeps (Supplementary Fig. 23). Consequently, long-term potentiation and depression characteristics are achieved with the application of positive and negative voltage pulses (Fig. 4a). The retention of 3-bit resistance states are further examined, exhibiting stable retention over 3,000 s (Fig. 4b). The device also exhibits a fast response time of 60 ns (Fig. 4c). Additional retention tests over multiple devices and extrapolated to 10 years (Supplementary Figs. 24 and 25) and the cycle-to-cycle and device-to-device variation tests (Supplementary Figs. 9 and 10) are performed, suggesting good stability.

The analogue electrical resistive switching characteristic is attributed to the migration of $O^{2-}$ ions in $CuO_x$ near the $I_xT_yO_{1-x-y}/CuO_x$ interface, resulting in the alteration of the interface barrier height (Fig. 4d–f). Owing to the small applied voltage, the migration dynamics occur only in the region close to the $I_xT_yO_{1-x-y}/CuO_x$ interface (top region), whereas the region near the Pd/$CuO_x$ interface (bottom region) experiences negligible events. At the initial state, an intermediate conductance state is formed owing to the randomly distributed $O^{2-}$ ions and defect-induced trap sites in the $CuO_x$ thin film. At the onset of the application of a positive voltage, $O^{2-}$ ions move into the $I_xT_yO_{1-x-y}$ electrode, leaving behind vacant sites ($V_O^{\cdot\cdot}$) with relative positive charges in the $CuO_x$ layer near the $I_xT_yO_{1-x-y}$ electrode. This results in a net doping effect, reducing the barrier height seen by electrons towards the $I_xT_yO_{1-x-y}$ electrode and thereby decreasing the device resistance. Conversely, with the application of a negative voltage, $O^{2-}$ ions move back from the $I_xT_yO_{1-x-y}$ electrode into the $CuO_x$ layer, compensating the relative charge, raising the barrier height and increasing the device resistance. This proposed mechanism is further supported by area-dependent measurements (Supplementary Fig. 15), comparison of oxygen-rich and oxygen-deficient devices' behaviours (Supplementary Figs. 26 and 27 and Supplementary Note 7), and humidity-dependent measurements[28,29,34,35] (Supplementary Fig. 12 and Supplementary Note 3).

The switching dynamics is further elucidated by the in situ EELS–STEM experiment (Fig. 4g). The $CuO_x$ layer was divided into top and bottom segments, adjacent to the $I_xT_yO_{1-x-y}$ and Pd electrodes, respectively. The O and Cu intensity line profiles (Fig. 4h) and the time-series energy-loss near-edge structure spectra (Fig. 4i,j) are utilized to identify ion migration and valence changes at different times. After applying small positive voltage pulses (0.1 V), a slight decrease in the O K-edge pre-peak was observed in the top region of the $CuO_x$ layer (Fig. 4i), indicating a decrease in the oxidation state[33]. Concurrently, the O intensity line profile (left) shows an obvious decrease in the top region, whereas the Cu intensity line profile (right) does not show any observable change (Fig. 4h). However, the variations are inapparent in the bottom region (Fig. 4j). These observations suggest that only the $O^{2-}$ ions in the top region migrate into the $I_xT_yO_{1-x-y}$ electrode under the small voltage. In addition, the Cu-$L_3$ edge exhibited a slight left shift in response to positive pulses only in the top region (Fig. 4i,j), consistent with the decrease in the oxidation state. Conversely, with the application of negative voltage pulses, both O K-edge pre-peak intensity and chemical shift in the Cu-$L_3$ edge at the top region of $CuO_x$ revert.

## Cortical neuron dynamics

The cortical neuron dynamics is accessed within a bias of 1.3 V to 2 V, exhibiting electrical graded neuron and LIF behaviour under continuous electrical pulses. The electrical behaviour of the device initiating firing above a current threshold is presented in Fig. 5a, where there is a specific rate of current increase required before it can reach the pre-defined threshold (10 μA). In this case, we see that a minimum of 1.3 V is required before LIF behaviours can be observed. The duration during which the current reaches this threshold is known as the leaky-integration period. On removing the electrical pulse stimuli, the current returns to its initial state (refractory period). With an increased voltage amplitude (1.3 V ≤ $V$ ≤ 1.7 V), the pulses required for firing significantly decrease. The pulse amplitude- and pulse number-dependent firing conditions of the device are summarized in Fig. 5b. In addition, it can be seen that the firing is also highly dependent on the pulse width and frequency (Fig. 5c). With a larger pulse width and/or higher frequency, a smaller pulse number is required for firing. Stable and repeatable cortical neuron dynamics are shown in Supplementary Figs. 9 and 10, indicating the suitability of the device for large-scale implementation. More systematic studies of the cortical neuron dynamics, including paired-pulse facilitation and depression ratio and LIF behaviours dependent on pulse amplitude/number/width/interval, are investigated (Supplementary Figs. 28–34).

The electrical LIF neuron characteristic is attributed to the modulation of barrier height as mobile $O^{2-}$ ions move in the $CuO_x$ layer, as well as electron-trapping dynamics. Owing to the large applied voltage, the $O^{2-}$ ion migration occurs across the entire $CuO_x$ layer. The device is initially in the HRS state, with defects randomly distributed throughout the $CuO_x$ layer (Fig. 5d). When positive voltage pulses are applied, the effective electron barrier from Pd to the $CuO_x$ layer decreases, prompting electrons to be injected. Part of the electrons that move

**Fig. 4 | UANV device operating in the cortical synapse dynamics. a**, Pulse switching of long-term potential and depression characteristics (100 cycles) programmed with potentiation pulse amplitude and duration of 0.5 V and 50 ms, and depression pulse amplitude and duration of −0.5 V and 50 ms, respectively. **b**, Non-volatile multilevel resistance states (eight clearly separated states) programmed by voltage pulse amplitude and duration of 0.5 V and 50 ms, respectively, with a read voltage of 10 mV. **c**, Current response speed in the CS dynamics device, demonstrating a fast response time of 60 ns. **d**, Schematic illustrating the analogue electrical resistive switching characteristics in the device in CS dynamics at the initial stage. An intermediate conductance state is formed owing to the randomly distributed $O^{2-}$ ions and trap sites in the $CuO_x$ thin film. **e**, Schmatic illustrating the $O^{2-}$ ion migration under an applied positive voltage and the band diagram at LRS after the removal of bias. With the application of a positive voltage bias to the $I_xT_yO_{1-x-y}$ electrode, $O^{2-}$ ions migrate towards the $I_xT_yO_{1-x-y}$ electrode, whereas vacant sites are formed in the $CuO_x$ layer near the $I_xT_yO_{1-x-y}$ electrode. This results in a net doping effect, effectively lowering the electron barrier height seen from $CuO_x$ to $I_xT_yO_{1-x-y}$ and driving the device into LRS. **f**, Schmatic illustrating the $O^{2-}$ ion migration under an applied negative voltage and the band diagram at HRS after the removal of bias. With the application of a negative voltage at the $I_xT_yO_{1-x-y}$ electrode during the reset process, the $O^{2-}$ ions move back from the $I_xT_yO_{1-x-y}$ electrode into the $CuO_x$ layer, mitigating the relative positive charges and resetting the device back to HRS. **g**, STEM image of the sample with the region measured by EELS marked out. **h**, EELS mapping and O (left) and Cu (right) intensity line profiles before and after the set process. **i**,**j**, O K-edge and Cu-L edge in the top (**i**) and bottom (**j**) regions are plotted at different time steps corresponding to the set (positive bias) and reset (negative bias) process. The decrease in the O K-edge pre-peak and a left shift in the Cu-$L_3$ edge indicate the moving away of the $O^{2-}$ ions, whereas an increase in the O K-edge pre-peak and a right shift in the Cu-$L_3$ edge indicate the moving back of the $O^{2-}$ ions, especially in the top region.

https://doi.org/10.1038/s41565-025-01984-3

across the $CuO_x$ layer are trapped by the defect states, which serve as the electron trap sites. Meanwhile, $O^{2-}$ ions move towards the $I_xT_yO_{1-x-y}$/$CuO_x$ interface under the applied bias. The continuous migration of $O^{2-}$ ions into the $I_xT_yO_{1-x-y}$ electrode gradually lowers the effective barrier height due to the relative positive charge created (Fig. 5e). The continuous electron trapping and $O^{2-}$ ion migration processes correspond to the leaky-integration process. This effect is more pronounced with larger voltage pulse amplitudes owing to a significantly lowered effective barrier, and enhanced electron trapping and $O^{2-}$ ion migration processes (Fig. 5f). With the removal of the voltage pulses, the device enters the recovery stage, where electrons are de-trapped and the back-migration of $O^{2-}$ ions occurs (secondary role with slower dynamics; Fig. 5g). The proposed mechanism in cortical neuron dynamics is further supported by extended comparisons of O-rich and O-deficient devices (Supplementary Fig. 27 and Supplementary Note 7), as well as humidity-dependent and area-dependent measurements (Supplementary Figs. 12 and 15 and Supplementary Note 3).

Similarly, the dynamics of $O^{2-}$ ion migration and electron trapping/de-trapping are corroborated by in situ EELS–STEM characterization. The area measured is marked out in Fig. 5h. The elemental mapping and corresponding intensity line profiles are shown in Fig. 5i. Figure 5j,k shows the time-series energy-loss near-edge structure spectra of the

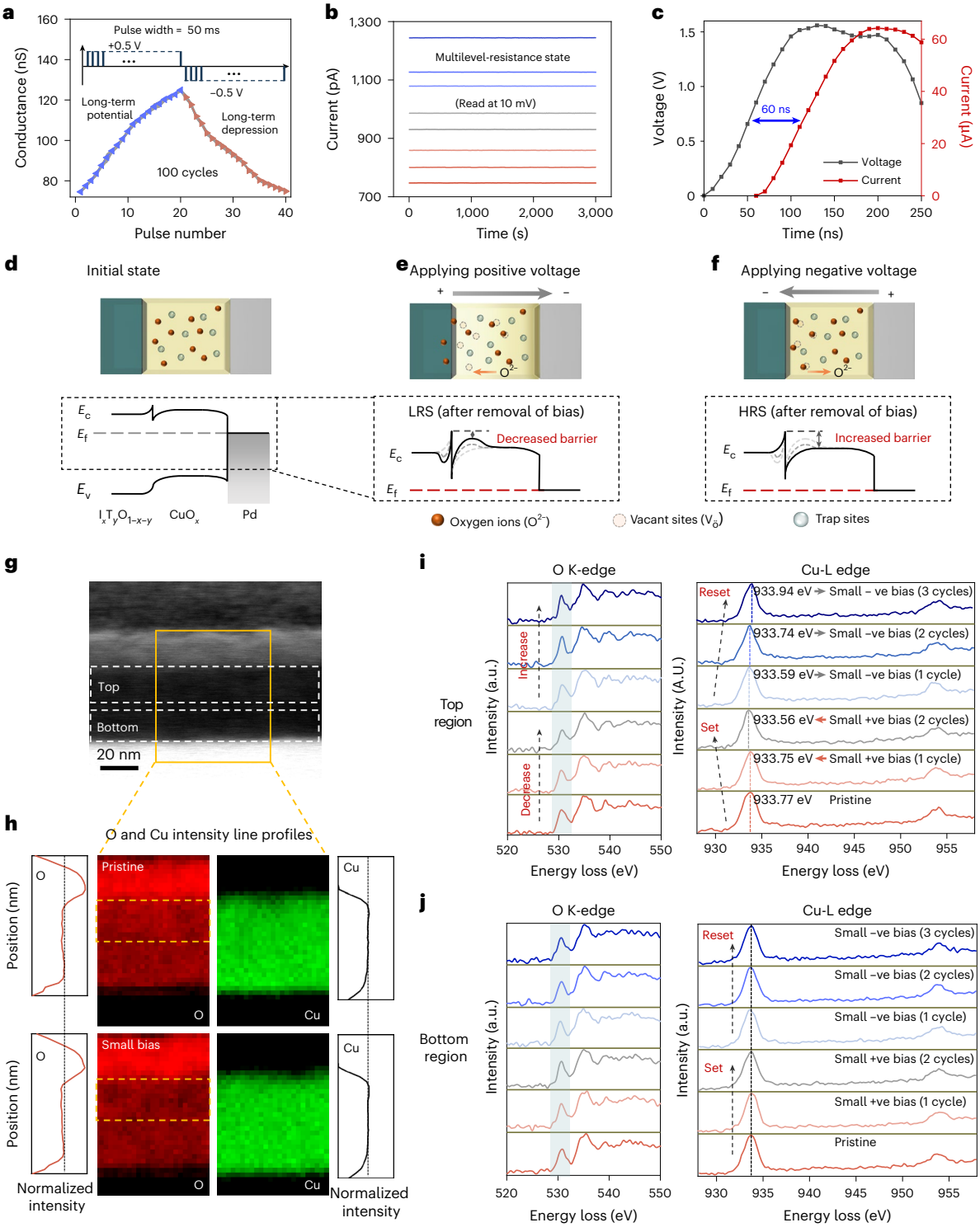

device at the top and bottom segments, respectively. A series of larger voltage pulses are applied, followed by the recovery process. In contrast to the small voltage applied, here a more significant reduction in the O K-edge pre-peak can be observed throughout the $CuO_x$ layer (Fig. 5j,k), which is more obvious in the top region (Fig. 5j). Furthermore, the O intensity line profile (left) within the $CuO_x$ layer decreases obviously, whereas the Cu intensity line profile (right) does not show much change (Fig. 5i). These observations indicate the substantial migration of $O^{2-}$ ions towards the $I_xT_yO_{1-x-y}$ electrode. Although the O concentration decrease typically leads to a reduction in the oxidation state and the valence state of the transition metal cations, it is counterintuitive that the Cu-$L_3$ edge shifts to the right in this case (Fig. 5j,k), which signifies an increase in the valence state. The abnormal rightward shift in the Cu-$L_3$ edge observed here is attributed to the trapping of a large number of injected electrons at the defect states, which significantly alters the charge distribution and chemical state of the Cu cations. In particular, the rightward shift in the Cu-$L_3$ edge is more pronounced in the bottom region near the Pd electrode, where electrons are initially injected. On removing the voltage pulses, a gradual increase in the O K-edge pre-peak and leftward shift in the Cu-$L_3$ edge across the entire $CuO_x$ layer are observed, indicating the reverse migration of $O^{2-}$ ions driven by the oxygen concentration gradient formed during the current potentiation stage and electron de-trapping process, recovering the device.

## AGVI system

An AGVI system utilizing the UANV device array to dynamically handle spatially frame-driven to spatiotemporally event-driven ever-changing scenarios is constructed. Figure 6a shows the optical micrograph of the device array. Further, an adaptive dynamic-control circuit is designed for the UANV device to access all the device dynamics depending on the scenario requirements, with ultralow power consumption. Details of accessing the different device dynamics by the dynamic-control circuit are provided in Supplementary Fig. 35 and Supplementary Note 8. This design allows the device array to be stacked for an ultra-adaptive and homogeneous vision system, schematically shown in Fig. 6b. A system prototype implemented with the UANV array and board-level dynamic-control circuitry is illustrated in Fig. 6c, enabling flexible device dynamic reallocation.

Examples of handling ever-changing dynamic and static traffic scenarios are further demonstrated based on our proposed AGVI system (Fig. 6d), with the results simulated using UANV cell behaviours extracted from our hardware prototype, including vehicle attribute-aware collision detection (scenario 1), motion direction prediction (scenario 2), traffic sign recognition (scenario 3) and speed-limit digit recognition (scenario 4), each with specific task demands. To address the different demands of each scenario with high efficiency and accuracy, the system intelligently shuttles between spiking visual network architectures (event-driven scenario processing) and non-spiking artificial visual network (frame-driven scenario processing) architectures with adapted UANV device dynamics and allocations (Fig. 6e).

Scenario 1 is to detect potential traffic incidents, including detecting collision risks and vehicle attributes (for example, colour and type). The system adapts to a spiking visual network architecture with a relatively large allocation of retina-like RSN dynamics to capture relatively high-resolution vehicle attributes and a smaller allocation of cortex-like cortical synapse and cortical neuron dynamics for cognitive processing. The RSN dynamic array first extracts and encodes the continuous motion information of the two target vehicles (trajectory, speed, motion direction and vehicle attributes) into spike maps, whereas filtering out the static background based on light intensity-based threshold spiking features (Fig. 6f and Supplementary Fig. 36). These spike maps are subsequently input to the cortical synapse and cortical neuron dynamic arrays for cognitive processing, achieving 92% high accuracy in detecting collision risks and identifying vehicle attributes. In scenario 2, the goal shifts to predicting the vehicle's motion in the next step direction, which requires more complex cortex-like cognitive processing but less retina-like sensing. Hence, more UANV devices are allocated to the cortical synapse and cortical neuron dynamics, whereas fewer devices are allocated to RSN dynamics compared with scenario 1. The RSN dynamic array encodes the 12 history motion steps into voltage spike signals, filtering the static background in real time. The voltage spike map output with the extracted motion trajectory (Fig. 6g) are then sent into the cortical synapse and cortical neuron dynamic arrays for future direction prediction, achieving a high accuracy of 92%.

Scenario 3 is to recognize different types of traffic sign, without focusing on the specific details (for example, exact speed limits). Therefore, only a small portion of the UANV devices is allocated to the RGN dynamics, whereas a larger portion is assigned to the CS dynamics. The RGN dynamic array filters red noise by generating smaller and faster-faded photocurrents for noisy red pixels than the photocurrent of blue target pixels, improving the image quality. These voltage maps are then sent to the cortical synapse dynamic array, achieving a 90% accuracy in recognizing noisy traffic signs (Fig. 6h). In scenario 4, the task is to recognize more detailed information on specific traffic signs, such as the speed-limit digits on the 'speed-limit' sign. To capture finer details of the digits, more UANV devices are allocated to the RGN dynamics and fewer devices are allocated to the cortical synapse dynamics owing to simpler recognition tasks. The system correctly classifies noisy speed-limit digits with a high accuracy of 91% (Fig. 6i). Details of the dataset, processing results and processing schemes for the four scenarios are provided in Supplementary Figs. 37–48 and Supplementary Notes 9–11.

## Conclusions

We report a UANV device that highly fuses four visual neuronal dynamics. The unique multi-dynamics in a single device presents superiorities compared with state-of-the-art emerging neuromorphic devices in terms of power consumption, adaptivity and scalability[6,14–18] (Extended Data Table 1 and Supplementary Table 1). The advanced functionalities and performances lead to a highly homogeneous AGVI system. To further evaluate the system's performance, the circuits supporting the complete hardware vision system are realized using a commercial

**Fig. 5 | UANV device operating in the cortical neuron dynamics. a**, Basic behaviours under voltage pulses with varied amplitudes (0.9 V to 1.7 V) and the pulse amplitude threshold for firing. **b**, Firing condition. **c**, Device characteristics with different applied pulse widths and intervals. **d**, Schematic illustrating the working principles in the device in CN dynamics at the initial stage. The energy band diagram is shown with the presence of $O^{2-}$ ions and trap sites randomly distributed across the $CuO_x$ layer. **e**, Schematic illustrating the working principles in the device in CN dynamics at the integrate-and-fire stage. Low LIF intensity ($1.3\ V \le V \le 1.5\ V$): under a positive voltage, the effective electron barrier from Pd to the $CuO_x$ layer decreases, prompting electrons to be injected. Electrons that move across the $CuO_x$ layer are trapped by the electron trap sites. Meanwhile, $O^{2-}$ ions gradually migrate into the $I_xT_yO_{1-x-y}$ electrode, further causing a reduction in the interfacial barrier height. **f**, High LIF intensity ($V \ge 1.7\ V$): under a larger applied voltage, the injection of electrons is enhanced, accompanied by enhanced $O^{2-}$ ion migration and electron-trapping processes. **g**, Recovery stage: with the removal of the voltage pulses, the device goes into the recovery stage. In this stage, the electrons start to get de-trapped from the trap sites. At the same time, the back-migration of $O^{2-}$ ions from the $I_xT_yO_{1-x-y}$ electrode back into bulk $CuO_x$ occurs, mitigating the relative positive charge distribution due to the vacant sites. **h**, STEM image of the sample with the region imaged by EELS marked out. **i**, EELS mapping and O (left) and Cu (right) intensity line profiles before and after the application of a large bias. **j**,**k**, O K-edge and Cu-L edge at top (**j**) and bottom (**k**) regions are plotted at different time steps corresponding to the application of a bias and the recovery process.

https://doi.org/10.1038/s41565-025-01984-3

180 nm complementary metal–oxide–semiconductor process design kit (Supplementary Figs. 49 and 50, Supplementary Tables 2–5 and Supplementary Note 12). Our system achieves a power efficiency of up to 6.26 trillion operations per second per watt for spiking-based sensory computing and 67.89 trillion operations per second per watt for non-spiking-based sensory computing, with an area efficiency of up to 3.96 MOPS/F$^2$, demonstrating superior performance compared with the state-of-the-art reported general vision systems[5,36,37] (Supplementary Table 6). Further optimizations may include (1) improving device uniformity and enhancing mode controllability for practical noisy environments; (2) implementing a complete hardware demonstration on a chip-scale platform. The synergy between AGVI and the UANV device marks a critical milestone in the journey towards achieving truly low-power, compact adaptive vision intelligence for edge devices.

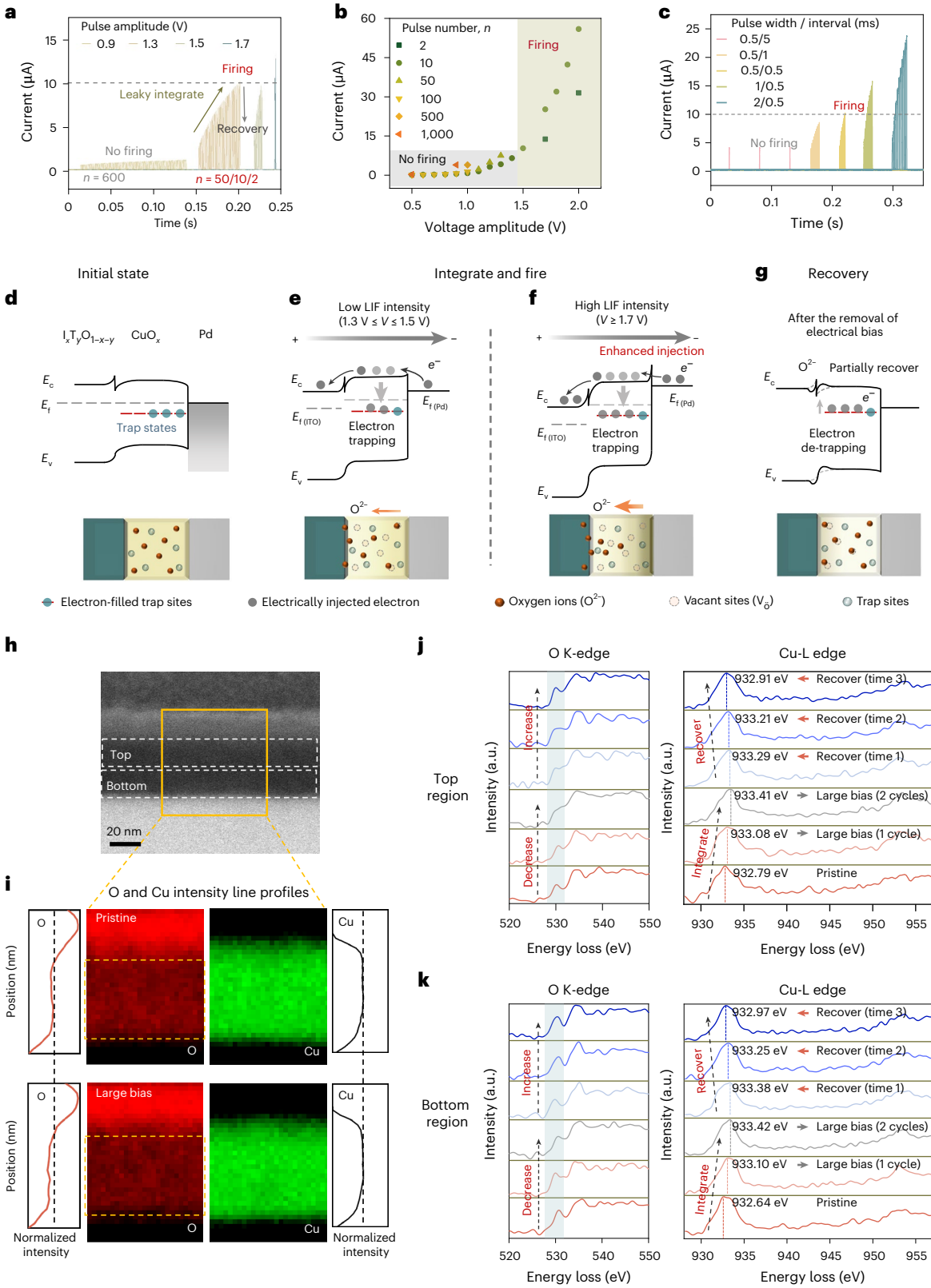

https://doi.org/10.1038/s41565-025-01984-3

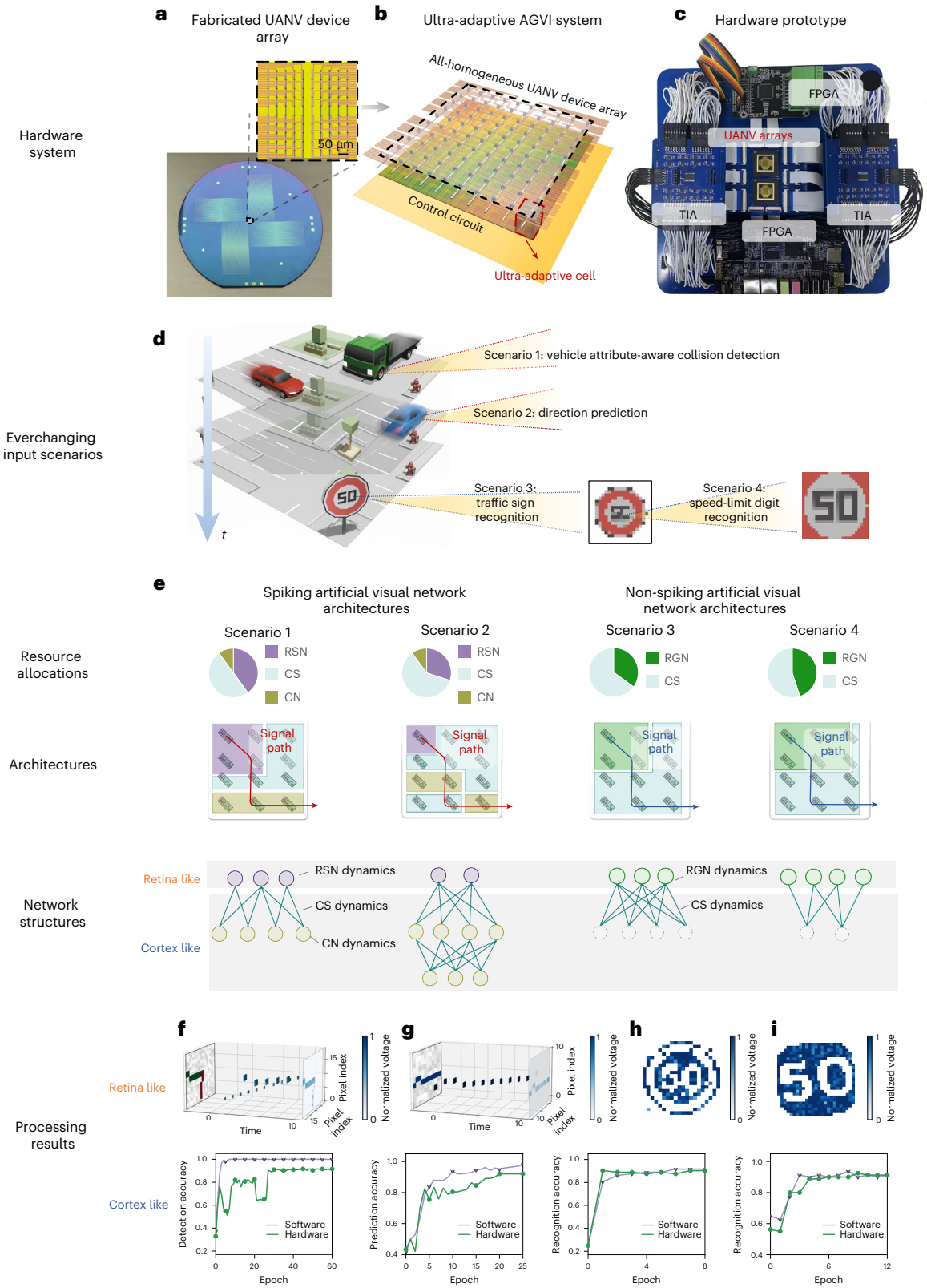


**Fig. 6 | AGVI system. a**, Optical micrograph of the UANV device array. **b**, Stacked architecture of the AGVI system with ultrahigh adaptivity, with each cell comprising a UANV device stacked on a dynamic-control circuit. **c**, Prototype hardware system constructed with the UANV array and board-level dynamic-control circuitry. FPGA, field-programmable gate array; TIA, transimpedance amplifier. **d**, Examples of ever-changing dynamic and static traffic scenarios, including vehicle attribute-aware collision detection (scenario 1), motion direction prediction (scenario 2), traffic sign recognition (scenario 3) and speed-limit digit recognition (scenario 4), each with specific task demands. **e**, Adaptive hardware architectures with different UANV device dynamics allocations, and the corresponding visual networks. **f**–**i**, Processing results of scenario 1 (**f**), scenario 2 (**g**), scenario 3 (**h**) and scenario 4 (**i**), including the retina-like sensing and cortex-like recognition results.

## Online content

Any methods, additional references, Nature Portfolio reporting summaries, source data, extended data, supplementary information, acknowledgements, peer review information; details of author contributions and competing interests; and statements of data and code availability are available at https://doi.org/10.1038/s41565-025-01984-3.

## References


1. Pinto, L. et al. Task-dependent changes in the large-scale dynamics and necessity of cortical regions. *Neuron* **104**, 810–824. e819 (2019).
2. Juusola, M., French, A. S., Uusitalo, R. O. & Weckström, M. Information processing by graded-potential transmission through tonically active synapses. *Trends Neurosci.* **19**, 292–297 (1996).
3. Joselevitch, C. Human retinal circuitry and physiology. *Psychol. Neurosci.* **1**, 141–165 (2008).
4. Haag, J. & Borst, A. Encoding of visual motion information and reliability in spiking and graded potential neurons. *J. Neurosci.* **17**, 4809–4819 (1997).
5. Pei, J. et al. Towards artificial general intelligence with hybrid Tianjic chip architecture. *Nature* **572**, 106–111 (2019).
6. Zhou, F. et al. Optoelectronic resistive random access memory for neuromorphic vision sensors. *Nat. Nanotechnol.* **14**, 776–782 (2019).
7. Huang, H. Fully integrated multi-mode optoelectronic memristor array for diversified in-sensor computing. *Nat. Nanotechnol.* **20**, 93–103 (2025).
8. Kumar, S., Williams, R. S. & Wang, Z. Third-order nanocircuit elements for neuromorphic engineering. *Nature* **585**, 518–523 (2020).
9. Mahmoud, S. A. A new current-mode analog multiplier circuit. In *International Midwest Symposium on Circuits and Systems* 130–133 (IEEE, 2009).
10. Låte, E., Vatanjou, A. A., Ytterdal, T. & Aunet, S. Comparative analysis of flip-flop architectures for subthreshold applications in 28 nm FDSOI. In *Nordic Circuits and Systems Conference: NORCHIP & International Symposium on System-on-Chip* 1–4 (IEEE, 2015).
11. Chen, X. et al. CMOS-based area-and-power-efficient neuron and synapse circuits for time-domain analog spiking neural networks. *Appl. Phys. Lett.* **122**, 053502 (2023).
12. Nguyen, V. T., Trinh, Q. K., Zhang, R. & Nakashima, Y. STT-BSNN: an in-memory deep binary spiking neural network based on STT-MRAM. *IEEE Access* **9**, 151373–151385 (2021).
13. Park, J. H., Tan, J. S. Y., Wu, H., Dong, Y. & Yoo, J. 1225-channel neuromorphic retinal-prosthesis SoC with localized temperature-regulation. *IEEE Trans. Biomed. Circuits Syst.* **14**, 1230–1240 (2020).
14. Indiveri, G., Chicca, E. & Douglas, R. A VLSI array of low-power spiking neurons and bistable synapses with spike-timing dependent plasticity. *IEEE Trans. Neural Netw.* **17**, 211–221 (2006).
15. Han, J.-K. et al. 3D stackable broadband photoresponsive InGaAs biristor neuron for a neuromorphic visual system with near 1V operation. In *International Electron Devices Meeting* 1–4 (IEEE, 2021).
16. Wang, X. et al. Vertically integrated spiking cone photoreceptor arrays for color perception. *Nat. Commun.* **14**, 3444 (2023).
17. Mennel, L. et al. Ultrafast machine vision with 2D material neural network image sensors. *Nature* **579**, 62–66 (2020).
18. Fu, Y. et al. Reconfigurable synaptic and neuronal functions in a V/$VO_x$/$HfWO_x$/Pt memristor for nonpolar spiking convolutional neural network. *Adv. Funct. Mater.* **32**, 2111996 (2022).
19. Dang, B. et al. Reconfigurable in-sensor processing based on a multi-phototransistor–one-memristor array. *Nat. Electron.* **7**, 991–1003 (2024).
20. Huang, H. et al. Fully integrated multi-mode optoelectronic memristor array for diversified in-sensor computing. *Nat. Nanotechnol.* **20**, 93–103 (2025).
21. John, R. A. et al. Optogenetics inspired transition metal dichalcogenide neuristors for in-memory deep recurrent neural networks. *Nat. Commun.* **11**, 3211 (2020).
22. Wu, Q. et al. Spike encoding with optic sensory neurons enable a pulse coupled neural network for ultraviolet image segmentation. *Nano Lett.* **20**, 8015–8023 (2020).
23. Chen, J. et al. Optoelectronic graded neurons for bioinspired in-sensor motion perception. *Nat. Nanotechnol.* **18**, 882–888 (2023).
24. Seo, S. et al. Artificial optic-neural synapse for colored and color-mixed pattern recognition. *Nat. Commun.* **9**, 5106 (2018).
25. Ahmed, T. et al. Fully light-controlled memory and neuromorphic computation in layered black phosphorus. *Adv. Mater.* **33**, e2004207 (2021).
26. Hou, Y. X. et al. Large-scale and flexible optical synapses for neuromorphic computing and integrated visible information sensing memory processing. *ACS Nano* **15**, 1497–1508 (2021).
27. Valov, I. & Tsuruoka, T. Effects of moisture and redox reactions in VCM and ECM resistive switching memories. *J. Phys. D: Appl. Phys.* **51**, 403001 (2018).
28. Tsuruoka, T. et al. Effects of moisture on the switching characteristics of oxide-based, gapless-type atomic switches. *Adv. Funct. Mater.* **22**, 70–77 (2011).
29. Milano, G. et al. Water-mediated ionic migration in memristive nanowires with a tunable resistive switching mechanism. *ACS Appl. Mater. Interfaces* **12**, 48773–48780 (2020).
30. Milano, G. et al. Ionic modulation of electrical conductivity of ZnO due to ambient moisture. *Adv. Mater. Interfaces* **6**, 1900803 (2019).
31. Duan, T., Wang, W., Cai, S. & Zhou, Y. On-chip light-incorporated in situ transmission electron microscopy of metal halide perovskite materials. *ACS Energy Lett.* **8**, 3048–3053 (2023).
32. Cai, S. et al. Development of in situ optical-electrical MEMS platform for semiconductor characterization. *Ultramicroscopy* **194**, 57–63 (2018).
33. Tan, H., Verbeeck, J., Abakumov, A. & Van Tendeloo, G. Oxidation state and chemical shift investigation in transition metal oxides by EELS. *Ultramicroscopy* **116**, 24–33 (2012).
34. Lübben, M., Wiefels, S., Waser, R. & Valov, I. Processes and effects of oxygen and moisture in resistively switching $TaO_x$ and $HfO_x$. *Adv. Electron. Mater.* **4**, 1700458 (2017).
35. Cho, D. Y., Luebben, M., Wiefels, S., Lee, K. S. & Valov, I. Interfacial metal-oxide interactions in resistive switching memories. *ACS Appl. Mater. Interfaces* **9**, 19287–19295 (2017).
36. Dudek, P. et al. Sensor-level computer vision with pixel processor arrays for agile robots. *Sci. Robot.* **7**, eabl7755 (2022).
37. Zhong, X., Law, M.-K., Tsui, C.-Y. & Bermak, A. A fully dynamic multi-mode CMOS vision sensor with mixed-signal cooperative motion sensing and object segmentation for adaptive edge computing. *IEEE J. Solid-State Circuits* **55**, 1684–1697 (2020).


**Publisher's note** Springer Nature remains neutral with regard to jurisdictional claims in published maps and institutional affiliations.

**Open Access** This article is licensed under a Creative Commons Attribution-NonCommercial-NoDerivatives 4.0 International License, which permits any non-commercial use, sharing, distribution and reproduction in any medium or format, as long as you give appropriate credit to the original author(s) and the source, provide a link to the Creative Commons licence, and indicate if you modified the licensed material. You do not have permission under this licence to share

adapted material derived from this article or parts of it. The images or other third party material in this article are included in the article's Creative Commons licence, unless indicated otherwise in a credit line to the material. If material is not included in the article's Creative Commons licence and your intended use is not permitted by statutory regulation or exceeds the permitted use, you will need to obtain permission directly from the copyright holder. To view a copy of this licence, visit http://creativecommons.org/licenses/by-nc-nd/4.0/.

© The Author(s) 2025

[1]School of Microelectronics, Southern University of Science and Technology, Shenzhen, China. [2]Department of Applied Physics, The Hong Kong Polytechnic University, Hong Kong, China. [3]School of Integrated Circuits, Harbin Institute of Technology (Shenzhen), Shenzhen, China. [4]Beijing Pixelcore Technology Co. Ltd, Beijing, China. [5]These authors contributed equally: Jiayi Xu, Biyi Jiang, Weizhen Wang. ✉e-mail: songhua.cai@polyu.edu.hk; liyd3@sustech.edu.cn; zhoufc@sustech.edu.cn

## Methods

### Device fabrication

A 30-nm-thick Pd bottom electrode was deposited via electron-beam evaporation (base pressure of $5 \times 10^{-6}$ mbar, deposition pressure of $5 \times 10^{-6}$ mbar and deposition rate of 0.59 Å $s^{-1}$) and patterned with optical lithography, followed by lift-off. Subsequently, a 40 nm $CuO_x$ layer was deposited by radio-frequency sputtering in a pure argon atmosphere (base pressure of $1 \times 10^{-8}$ Torr, deposition pressure of 7 mTorr and deposition rate of 0.23 Å $s^{-1}$) and patterned through optical lithography, followed by lift-off. A 30-nm transparent $I_xT_yO_{1-x-y}$ top electrode was similarly patterned and deposited by direct-current sputtering in an argon–oxygen mixed atmosphere ($Ar:O_2 = 50:1$; base pressure of $1 \times 10^{-8}$ Torr, deposition pressure of 3 mTorr and deposition rate of 0.3 Å $s^{-1}$), followed by lift-off.

### Materials characterization

The X-ray photoelectron spectroscopy and ultraviolet photoelectron spectroscopy measurements were conducted using a multifunctional X-ray photoelectron spectroscopy analysis platform (ESCALAB $Xi^+$, ThermoFisher). The transmission and absorption spectra were measured using an ultraviolet–visible–near-infrared spectrophotometer (750s, Lambda).

### Technology computer-aided design simulation

Sentaurus software is used for device simulation. For the optical model, the ray-tracing method is used to simulate the normal incidence of plane waves from the top, whereas the effect of material refractive index in each region is considered to simulate the optical absorption distribution in each region. The electrical model is taken from the energy band diagram measured from the ultraviolet photoelectron spectroscopy results. The Fermi–Dirac distribution was used. The carrier concentrations of $CuO_x$ and $I_xT_yO_{1-x-y}$ used in the simulation are $10^{18}$ and $5 \times 10^{18}$ $cm^{-3}$, respectively. The mobility model and composite model used are the doping dependence model and the Shockley–Read–Hall model, respectively. A heterojunction is formed at the junction of the $CuO_x$ and $I_xT_yO_{1-x-y}$ layers. To solve for the tunnelling current, non-local tunnelling is used to consider the tunnelling effect of electrons in the conduction band. The interface is considered as the centre, and the tunnelling current is obtained by integrating the current density over 10 nm of length.

To modulate the interface trap-state dynamics, we adopted the physical interface models. Finally, to obtain the solution, a transient simulation is adopted. This is because the direct addition of strong light at the beginning of the solution will cause convergence issues and solving the continuity equation; therefore, the slope is used to gradually impose the light to the target value to accelerate the convergence.

### Optoelectronic measurements

For RSN dynamics, the optical spiking measurements were performed with lasers (LL375/LL450/LL520/LL638/LL808/LL1064, CCRAMAN), a transresistance amplifier (SR570, Stanford Research Systems) and a digital storage oscilloscope (MDO34, Tektronix). During these measurements, the Pd electrode was grounded. For RGN dynamics, the optical current response measurements were performed with an arbitrary waveform generator (AFG31102, Tektronix) for pulsed laser control and a Keithley 2636B source meter. During these measurements, the indium tin oxide electrode was grounded. For cortical synapse dynamics, the direct current voltage sweep electrical measurements were performed with a Keithley 2636B source meter, with the Pd electrode grounded. The pulse measurements in the cortical synapse and cortical neuron dynamics were performed with an arbitrary waveform generator (AFG31102, Tektronix), a transresistance amplifier (SR570, Stanford Research Systems) and a digital storage oscilloscope (MDO34, Tektronix). During these measurements, the Pd electrode was grounded.

### In situ STEM

In situ STEM sample preparation: the cross-sectional transmission electron microscopy specimens were prepared using a dual-beam focused-ion-beam platform (Helios 5CX, Thermo Fisher). Protection layers with a thickness of 20 nm and 300 nm were deposited sequentially on the top electrode of the devices by electron- and ion-beam-deposited Pt, and the latter was used for electric connection from the chip's electrodes to the sample lamella. 30 kV operation voltage and 0.1–24 nA working current of gallium-ion beam were used for lamella preparation. The lamella was then lifted out from the substrate and transferred to the custom-made in situ optical–electrical microelectromechanical system chip. The top and bottom electrodes of the cross-sectional device lamella were welded with two microelectrodes of the microelectromechanical system chip by ion-beam Pt deposition. The observation area of the device lamella was located above the observation window of the microelectromechanical system chip and thinned to less than 100 nm with a 40–790 pA gallium-ion beam. The surface amorphous layer was removed through finely polishing using a gallium-ion beam with 2 kV accelerating voltage and 39 pA working current.

In situ STEM characterization: the custom-made in situ optical–electrical microelectromechanical system chip with the as-prepared device lamella was loaded onto a DENS solutions double-tilt in situ holder. This holder was connected with a Keithley 2612B dual-channel source measure unit through an interconnection box. One channel of the source measure unit was used to control the on-chip micro-light-emitting diode (LED) as the light source, whereas the other channel was connected to the device lamella for electrical testing. The wavelength of the micro-LED is 470 nm, and the working forward current and voltage are 10 mA and 3.3 V, respectively. As the input power of the micro-LED is only about 33 mW, the device lamella can quickly reach a steady state with little drifting during in situ illumination testing. In situ STEM observations were carried out on an aberration-corrected STEM microscope operating at 300 kV (Spectra 300, Thermo Fisher). The convergence half-angle of the electron probe is 29.9 mrad, and the collection half-angle for high-angle annular dark-field STEM imaging was from 57 mrad to 200 mrad. The dwell time for each pixel was 3 µs and the size for one STEM image is 2,048 × 2,048 pixels. The EELS datasets were collected in the STEM mode using a Gatan Continuum K3 HR imaging filter with a K3 direct electron detection camera, the acquisition energy range is from 419 eV to 1,040 eV with a dispersion of 0.18 eV per channel and an entrance aperture of 5 mm. The electron-beam current of the electron probe used to conduct in situ EELS–STEM characterizations was set as 20 pA to avoid electron-beam-induced artefacts.

## Data availability

The data that support the findings of this study are available from the corresponding authors upon reasonable request.

## Code availability

All codes used in the simulations supporting this Article are available from the corresponding authors upon reasonable request.

## Acknowledgements

This work was supported by the National Key Research and Development Project of China (grant 2023YFB2806300 to F.Z.), National Natural Science Foundation of China (grants 62104091 and 52273246 to F.Z. and 62174074 to Y.L.), Early Career Scheme (25305023 to S.C.) and the General Research Fund (no. 15306122 to S.C.) from the Hong Kong Research Grants Council, Shenzhen Science and Technology Program (grants JCYJ20220530115204009 to F.Z. and JCYJ20220530115014032 to Y.L.), Zhujiang Young Talent Program (grant 2021QN02X362 to Y.L.) and the startup grants from the Department of Applied Physics, the Hong Kong Polytechnic

University (1-BDCM). We thank Z. Lu (Hefei Reliance Memory Ltd) for insightful discussions, and SUSTech SME-Pixelcore Neuromorphic In-sensor Computing Joint Laboratory for experimental support in this work.

## Author contributions

F.Z. conceived and supervised the project. J.X., Z.G., J.G. and X.H. performed the experiments, including the device fabrication and characterization. B.J., L.L. and L.R. performed the simulations and designed the hardware system. W.W. and S.C. performed the in situ STEM. J.X., B.J., J.Q., L.L., S.C., Y.L. and F.Z. analysed the data. F.Z., Y.L., S.C., B.J. and J.X. co-wrote the paper.

## Competing interests

The authors declare no competing interests.

## Additional information

**Extended data** is available for this paper at https://doi.org/10.1038/s41565-025-01984-3.

**Supplementary information** The online version contains supplementary material available at https://doi.org/10.1038/s41565-025-01984-3.

**Correspondence and requests for materials** should be addressed to Songhua Cai, Yida Li or Feichi Zhou.

**Peer review information** *Nature Nanotechnology* thanks Nazek El-Atab and Ilia Valov for their contribution to the peer review of this work.

**Reprints and permissions information** is available at www.nature.com/reprints.

https://doi.org/10.1038/s41565-025-01984-3

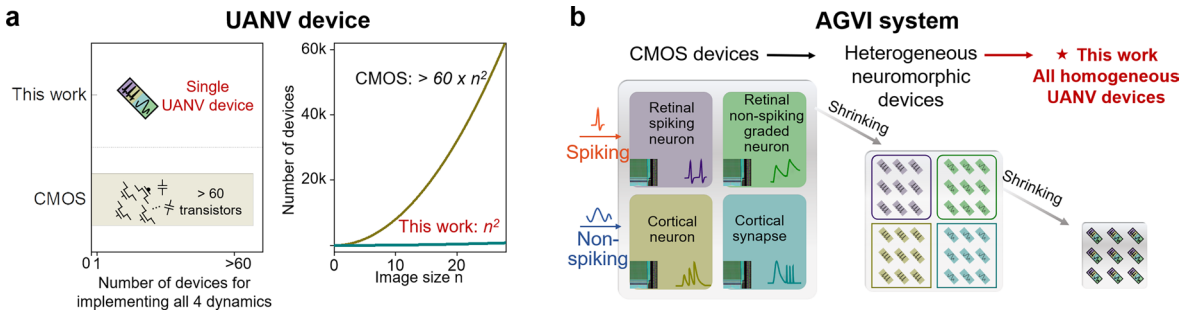


**Extended Data Fig. 1 | Comparisons of our UANV device and AGVI system with the state-of-the-art solutions. a**) UANV device melding the functionalities equivalent to those required by more than 60 devices in a conventional CMOS approach, dramatically reducing the devices required when image size increases. **b**) Illustration showing that CMOS-based and heterogeneous-integrated neuromorphic device-based general intelligent vision chips have much larger complexity and lower area efficiency as compared to the AGVI chip implemented with homogeneous UANV devices reported in this work.

https://doi.org/10.1038/s41565-025-01984-3

**Extended Data Table 1 | Comparisons of the state-of-the-art emerging neuromorphic devices with our UANV device**

| | | [14] | [15] | [16] | [6] | [17] | [18] | [19] | [20] | This work |
|---|---|---|---|---|---|---|---|---|---|---|
| **Configuration** | | CMOS circuits | InGaAs biristor + capacitor | Photoristor + memristor + Capacitor | $MoO_x$ optoelectronic RRAM | $MoS_2$ phototransistor | $V/VO_x/HfWO_x/Pt$ + capacitor | Phototransistor + $Ta/TaO_x/NbO_x/W$ + Capacitor | $TiN/ZnO/TiO_x/Pd$ | $Pd/CuO_x/I_xT_yO_{1-x-y}$ |
| | | > 20T + 1C | 1R+1C | 1T+1R+1C | 1R | 1T | 1R+1C | 1T+1R+1C | 1R | 1R (single device) |
| **Reconfigurability (dynamics)** | | Only RSN dynamic | | | Only RGN dynamic | | Only CS and CN dynamics | Only RSN and RGN dynamics | Only RGN and CS dynamics | **Ultrahigh** (RSN+RGN+CS+CN dynamics) |
| **Sensory computing capability** | | **Only spiking in-sensor computing** | | | **Only non-spiking in-sensor computing** | | **Only spiking and non-spiking in-memory computing** | **Only spiking and non-spiking in-sensor computing** | **Only non-spiking in-sensor and in-memory computing** | **Fully spiking/non-spiking in-sensor/in-memory reconfigurable** |
| **Photoresponsive** | | - | 520-1550 nm | 360-532 nm | 365 nm | 660 nm | No | 450-800 nm | 405-650 nm | **375 nm – 1064 nm** |
| **Program/ read voltage** | **RSN** | 3.3 V | 1.22V/1.22V | 0.2V/ 0.2V | Not support | | Not support | 1.5 V/ 1.5 V | Not support | **0 V/ 0 V** |
| | **RGN** | Not support | | | 0.1 V/ 0.1 V | -3 - 3 V/ 0.1 V | | 1 V/ 1 V | 0.3 V/ 0.3 V | **0.04 V/ 0.04 V** |
| | **CS** | Not support | | | | | 3 V/ 1.1 V | Not support | 0.5 V/ 0.2 V | **0.1 V/ 0.001 V** |
| | **CN** | Not support | | | | | 3 V/ 1.1 V | Not support | | **1.3 V/ 1.3 V** |
| **Electrical energy consumption per operation** | **RSN** | 900 pJ | 270 pJ | 30 pJ | Not support | | Not support | - | Not support | **0 pJ** |
| | **RGN** | Not support | | | 6.6 μJ | 6 nJ | Not support | - | 2 nJ | **42.5 fJ** |
| | **CS** | Not support | | | | | 60 fJ | Not support | 2 nJ | **14 fJ** |
| | **CN** | Not support | | | | | 1 nJ | Not support | | **0.35 nJ** |
| **CMOS-BEOL compatible** | | Yes | No | Yes | Yes | Yes | Yes | Yes | Yes | **Yes** |